ACCURACY ANALYSIS FOR FINITE-VOLUME DISCRETIZATION SCHEMES ON IRREGULAR GRIDS

BORIS DISKIN* AND JAMES L. THOMAS†

Abstract. A new computational analysis tool, downscaling test, is introduced and applied for studying the convergence rates of truncation and discretization errors of finite-volume discretization schemes on general irregular (e.g., unstructured) grids. The study shows that the design-order convergence of discretization errors can be achieved even when truncation errors exhibit a lower-order convergence or, in some cases, do not converge at all. The downscaling test is a general, efficient, accurate, and practical tool, enabling straightforward extension of verification and validation to general unstructured grid formulations. It also allows separate analysis of the interior, boundaries, and singularities that could be useful even in structured-grid settings. There are several new findings arising from the use of the downscaling test analysis. It is shown that the discretization accuracy of a common node-centered finite-volume scheme, known to be second-order accurate for inviscid equations on triangular grids, degenerates to first order for mixed grids. Alternative node-centered schemes are presented and demonstrated to provide second and third order accuracies on general mixed grids. The local accuracy deterioration at intersections of tangency and inflow/outflow boundaries is demonstrated using the DS tests tailored to examining the local behavior of the boundary conditions. The discretization-error order reduction within inviscid stagnation regions is demonstrated. The accuracy deterioration is local, affecting mainly the velocity components, but applies to any order scheme.

Key words. unstructured grids, irregular grids, finite-volume discretizations, accuracy analysis

AMS subject classifications. 65N12, 76M12

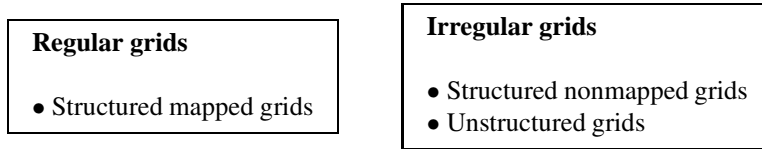| Regular grids	Irregular grids
• Structured mapped grids	• Structured nonmapped grids • Unstructured grids

FIG. 1.1. *Grid classification.*

1. Introduction. There is an increasing reliance on computational simulations in air-craft design practices, supplementing traditional analytic and experimental approaches. Verification and validation methodologies [20] are being developed to ensure the correct applicability of these approaches in practical applications on various grids. The following classification is used to characterize interior grids: grids with periodic (repeating) topological structure are called *structured*; grids derived by smooth mapping from structured grids with periodic metrics are called mapped grids. They are referred in this paper as *regular* grids (examples include, but are not limited to, grids derived from Cartesian ones: triangular grids obtained by the same diagonal splitting, stretched grids, smooth curvilinear grids, etc.). Grids with varying local topology are called *unstructured*, e.g., grids with the number of neighboring nodes changing from node to node; unstructured grids and nonmapped structured grids are considered *irregular*. Figure 1.1 illustrates this grid classification. Verification methodologies for regular grids, e.g., [17], are relatively well-developed in comparison to irregular grids, especially unstructured grids containing mixed elements or grids derived through agglomeration techniques. The summary of the latest of three Drag Prediction Workshops [14] illustrates the

problems associated with assessing errors in practical complex-geometry/complex-physics applications.

The two-dimensional (2D) primal meshes considered in this paper are composed of triangular and quadrilateral cells. The finite-volume discretization (FVD) schemes are derived from the integral form of a steady conservation law

$$\oint_{\Gamma} (\mathbf{F} \cdot \hat{\mathbf{n}}) \, d\Gamma = \iint_{\Omega} (f - S) \, d\Omega, \tag{1.1}$$

where f is a forcing function independent of the solution, S is a solution-dependent source function, Ω is a control volume with boundary Γ, $\hat{\mathbf{n}}$ is the outward unit normal vector, and $\mathbf{F}$ is the flux vector that may include viscous and/or inviscid contributions. The general FVD approach requires partitioning the domain into a set of non-overlapping control volumes and implementing numerically equation (1.1) over each control volume. The focus of this paper is node-centered FVD schemes, where solution values are stored at the mesh nodes; the proposed analysis techniques have already been applied in [25] to cell-centered FVD schemes.
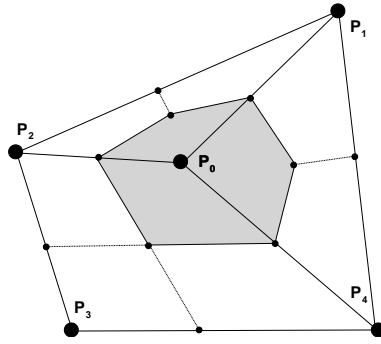

FIG. 1.2. *Median-dual partition for node-centered finite-volume discretizations. $P_0 - P4$ denote grid nodes. The control volume (dual cell) around P_0 is shaded.*

For 2D node-centered FVD schemes, a *median-dual* partition can be constructed by connecting the mass centers of the primal-mesh cells with the midpoints of the surrounding edges (Figure 1.2). These non-overlapping control volumes cover the entire computational domain and compose a mesh that is dual to the primal mesh.

The discrete solution is represented as a piecewise polynomial function; the polynomials are defined either within primal or dual cells. With discrete solution defined at the grid nodes, the fluxes at the dual-cell boundaries are reconstructed using these local polynomial representations. The discretization is applied at a sequence of refined grids satisfying the *consistent refinement property*. The property requires the maximum distance across primal and dual cells to decrease consistently with increase of the total number of grid points, N. In particular, the maximum distance should tend to zero as $N^{-1/2}$ in 2D computations. For three-dimensional (3D) unstructured grids, the consistent refinement property is studied in [25].

The main accuracy measure of any FVD scheme is the *discretization error*, E_d, defined as the difference between the exact discrete solution, Q^h, of the discretized equations (1.1) and the exact continuous solution, Q, to the differential conservation law

$$\nabla \mathbf{F} = f - S, \tag{1.2}$$

2

$$E_d = Q - Q^h; \tag{1.3}$$

Q is sampled at grid nodes.

A common approach to evaluate the accuracy of a FVD scheme is to monitor the convergence of *truncation errors*. Truncation error, E_t, measures the accuracy of the discrete approximation to the differential equations (1.2). For finite differences, it is defined as the residual obtained after substituting the exact solution Q into the discretized differential equations [15]. For FVD schemes, the traditional truncation error is usually defined from the time-dependent standpoint [23, 24]. In the steady-state limit, it is defined (e.g., in [10]) as the residual computed after substituting Q into the normalized discrete equations (1.1),

$$E_t = \frac{1}{|\Omega|} \left[-\iint\limits_{\Omega} \left(f^h - S^h \left(Q \right) \right) \, d\Omega + \oint\limits_{\Gamma} \left(\mathbf{F^h} \left(Q \right) \cdot \hat{\mathbf{n}} \right) \, d\Gamma \right], \tag{1.4}$$

where $\mathbf{F^h}$ is a reconstruction of the flux $\mathbf{F}$ at the boundary Γ, $|\Omega|$ is the measure of the control volume,

$$|\Omega| = \iint\limits_{\Omega} d\Omega, \tag{1.5}$$

f^h and S^h are, respectively, approximations of the forcing function f and the source function S on Ω, and the integrals are computed according to some quadrature formulas. Convergence of truncation errors has been applied as a FVD accuracy measure on both regular and irregular grids [5, 22]. On regular grids, this approach is well justified; the choice of scaling factor $\frac{1}{|\Omega|}$ ensures that truncation errors converge as $O(h^p)$ on sequences of consistently refined grids, where h is a characteristic meshsize and p is the design discretization-accuracy order of the method. However, the truncation-error convergence is often misleading for FVD schemes defined on irregular (e.g., unstructured) grids. Several studies, e.g., [19, 22], noted that 2nd-order convergence of truncation errors for some commonly used node-centered FVD schemes can be achieved only on grids with a certain degree of geometric regularity. Other studies, e.g., [10, 13], showed that such degradation of truncation-error convergence does not always imply a lower-order convergence of discretization errors. Examples in subsequent sections confirm that on irregular grids, the design-order discretization-error convergence can be achieved even when truncation errors exhibit a lower-order convergence or, in some cases, do not converge at all. Note that these results do not contradict to the Lax theorem, which states that consistency (convergence of truncation errors) and stability are sufficient (not necessary) for convergence of discretization errors. In fact, for some formally inconsistent FVD schemes, it has been rigorously proven that the discretization errors converge [7].

Although the convergence of irregular-grid truncation errors is not identical to the discretization-error convergence, it still can be monitored to indicate if the design order of the discretization accuracy can be achieved. On a sequence of irregular grids satisfying the consistent refinement property, the convergence order of truncation errors is typically less than the discretization-error convergence order by 1 for inviscid equations and by 2 for viscous equations.

The main *computational* tool introduced in this paper for evaluating accuracy of discretization schemes is a *downscaling (DS) test*. The test is performed for a known exact or manufactured solution. For a manufactured solution, the forcing functions are found by substituting this solution into the continuous governing equations and boundary conditions.

3

The DS test consists of a series of inexpensive computational experiments that account for local properties of the studied scheme; it is designed to provide estimates for the convergence orders of the discretization and truncation errors by comparing errors obtained on different scales. The DS test is a very general technique that can be applied to arbitrary grids and geometries. It can be tailored to study the discretization accuracy in the interior, at the boundary, and/or in vicinity of singularities. Analysis methods predicting the performance of DS tests have also been developed. Although, the computations presented in this paper are one- and two-dimensional, the analysis techniques and conclusions are fully extensible and have already been successfully applied in the three dimensions; some relevant 3D computations have been reported in [25]. While rigorous proofs of estimates for convergence of FVD truncation and discretization errors in realistic computations are still out of reach, the introduced practical analysis methods enable accurate and efficient accuracy assessment on various irregular grids, for various types of solutions and boundary conditions. Numerous examples reported here and in other recent publications ([8, 25]) confirm the predicting power and wide applicability of the DS-analysis.

The material in this paper is organized as follows. Section 2 describes the construction and application of DS tests for general FVD schemes on irregular grids. Section 3 introduces analytical methods for predicting convergence of discretization and truncation errors in a DS test. Section 4 includes one-dimensional examples providing insights into convergence of the discretization and truncation errors on irregular grids. Section 5 analyzes convergence for several sets of 2D equations and FVD schemes and corroborates the analysis with numerical tests performed on irregular triangular, quadrilateral, and mixed-element grids. In addition, the effects of flow singularities are analyzed; one-order reduction of the discretization accuracy is observed and explained for inviscid stagnation flows. The concluding Section 6 summarizes the demonstrated computational and analytical results and discusses complexity of the introduced FVD schemes.

2. Downscaling (DS) test. The purpose of the downscaling (DS) test is to predict the discretization and truncation-error convergence orders in computations performed on irregular grids satisfying the consistent refinement property. To apply a DS test, one first chooses a representative *manufactured* solution defined on the given computational domain.

The DS test requires numerical computations on a sequence of contracted domains zooming toward a focal point within the original computational domain (Figure 2.1). The choice of the focal-point location can be varied to study a typical interior discretization, a boundary discretization, or a particular singularity. Because the number of points in the DS-test domains is held (approximately) fixed, one can study solutions on grids with characteristic meshsizes much smaller than those affordable in computations with a globally-refined grid sequence.

There are at least two possible strategies for grid generation on these contracted domains: (1) The first strategy is termed "scaled grid"; with this strategy, the first (coarsest) computational domain is defined as a subdomain of the investigated global mesh containing the focal point; other (finer) domains and their mesh patterns are derived by scaling down this first domain (e.g., repeatedly multiplying all the distances from the focal point by a given factor, say, $1/2$ or $1/4$). (2) In an alternative, independent-grid approach, a new grid can be generated on each domain, assuming that the consistent refinement property is satisfied, i.e., the maximum distance across a grid cell is scaled down with the same rate as the diameter of the contracted domains.

The "scaled-grid" approach (sketch (a) in Figure 2.1) is especially useful for studying interior discretizations and straight boundaries. It is impractical for studies near a general (discretely defined) curvilinear boundary because the physical boundary shape should be preserved on each scale in the DS sequence (sketch (c) in Figure 2.1). In the DS test, the studied

(a) Scaled-grid approach

(b) Independent-grid approach
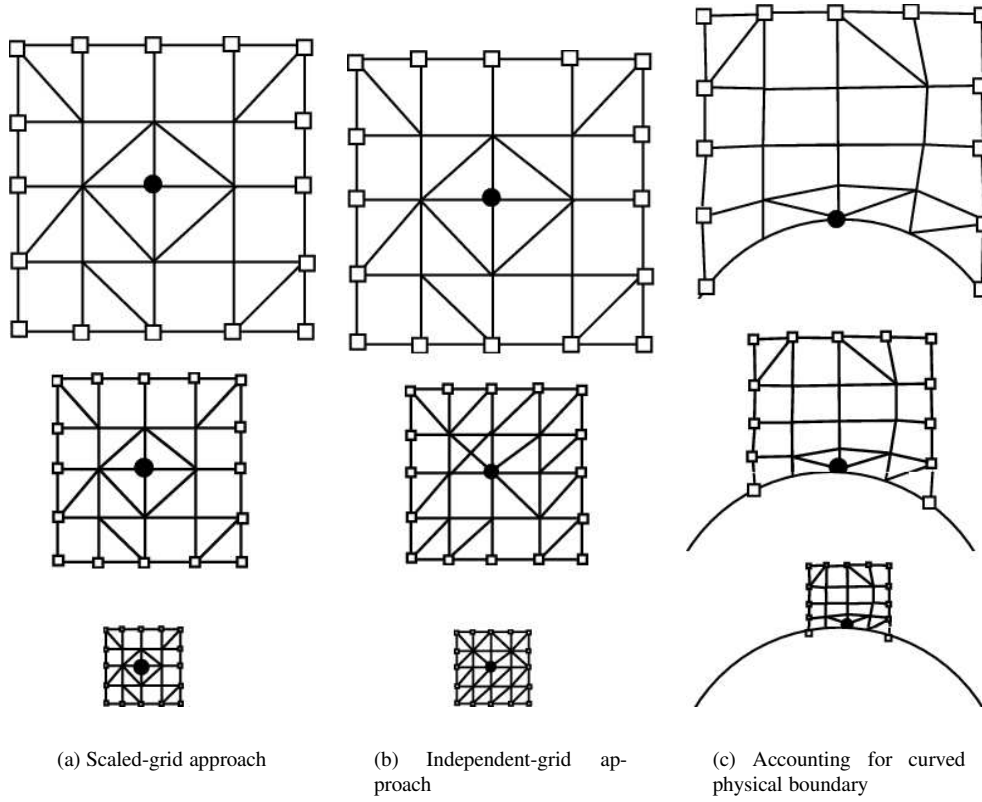
(c) Accounting for curved physical boundary

FIG. 2.1. *DS test: illustration of computational domains for studying the interior and general boundary. Black bullets mark the focal points; white squares mark the interface between the interior and the DS-test domain.*

FVD scheme is supplemented with a set of boundary conditions at the interface between the interior and the DS domain; overspecification from the known manufactured solution is a usual choice. The freedom to choose the focal point, the shape of domains, the type of boundary conditions, and the grid generation method greatly simplifies DS testing. In studying accuracy of discrete boundary conditions, i.e., placing the focal point at the physical boundary, the physical conditions are implemented at the studied boundary surface; overspecification can be applied at the interface between the interior and the DS domain (see sketches in Figure 2.1).

The DS test evaluates local truncation and discretization-error convergence orders by comparing errors obtained in computations on different scales. The DS convergence of truncation errors is an accurate indication of the truncation-error convergence (in the L_∞-norm) observed in global grid-refinement computations, providing the DS test samples all representative regions. Convergence of grid-refinement truncation errors measured in integral norms, e.g., L_1-norm, may be higher order because these norms are less sensitive to fluctuations occurring locally.

On grids with an increased regularity, the DS test may overestimate convergence of the discretization errors. Some global error accumulation may occur on such grids; because of its local nature and overspecified interface boundary conditions, the DS test is incapable to account for the global error accumulation. Our experience shows that on truly irregular multidimensional grids, errors produced locally dominate globally accumulated errors, and

the discretization-error estimates obtained in a DS test become sharp.

3. Analysis of discretization and truncation errors. In this section, we describe an analytical approach to estimating the convergence orders of the discretization and truncation errors on irregular grids.

3.1. Foundations of analysis. The analysis is performed for a known exact or manufactured solution. For a given FVD scheme, we define a *general residual function*

$$R(q) = \frac{1}{\beta} \left[\oint_{\Gamma} \left(\mathbf{F^h}(q) \cdot \hat{\mathbf{n}} \right) d\Gamma - \iint_{\Omega} \left(f^h - S^h(q) \right) d\Omega \right], \tag{3.1}$$

where q is a discrete function defined at the grid nodes; β is a scaling factor; at each control volume, the flux reconstruction $\mathbf{F^h}$ and the source approximation S^h are computed for q, using local polynomial approximation; and the outward unit normal $\hat{\mathbf{n}}$, the discrete force function f^h, and all integrals are approximated with certain accuracy by predefined methods. The general residual accounts for interior discretization and all boundary conditions. Note that by definition

$$R(Q^h) = 0 \tag{3.2}$$

and

$$R(Q) = \frac{|\Omega|}{\beta} E_t. \tag{3.3}$$

Recall that Q^h and Q are the exact discrete solution and a discrete (sampled-at-nodes) representation of the exact continuous solution, respectively. Substituting (1.3) into (3.2),

$$R(Q - E_d) = 0, \tag{3.4}$$

and assuming the discretization error to be small comparing to the exact continuous solution, Q, $(|E_d| << |Q|)$, we obtain

$$R(Q) - J(Q)E_d \approx 0, \tag{3.5}$$

where $J(Q)$ is the Jacobian of $R(q)$ computed for $q = Q$.

$$J(Q) = \frac{1}{\beta} \frac{\partial}{\partial q} \left(\left[\oint_{\Gamma} \left(\mathbf{F^h}(Q) \cdot \hat{\mathbf{n}} \right) d\Gamma + \iint_{\Omega} S^h(Q) d\Omega \right] \right). \tag{3.6}$$

Thus, the discretization error can be estimated as

$$E_d \approx J^{-1}(Q)R(Q), \tag{3.7}$$

The equation (3.7) is the main vehicle for relating discretization and truncation errors and for estimating the discretization-error convergence order. Note that the estimate does not depend on the scaling factor β, so β can be adjusted to simplify analysis. In particular, in the course of this paper, we choose

$$\beta = |\Gamma|, \tag{3.8}$$

6

where $|\Gamma| = |\Omega|^{(d-1)/d} = h^{d-1}$ is the measure of the control-volume boundary, d is the space dimension, and h is a characteristic diameter of the control volumes. Note, that with this scaling, the truncation error computed according to (1.4) relates to $R(Q)$ as

$$E_t = O\left(\frac{R(Q)}{h}\right). \tag{3.9}$$

Estimates of residual (and truncation-error) convergence are relatively easy to obtain for a given manufactured solution because the estimation does not require solution of discrete equations; residuals can be directly measured in computations. Thus, the main complexity of evaluation of the discretization-error convergence order rests with evaluation of the inverse Jacobian, which accounts for both interior and boundary discretizations. Example evaluations of the inverse Jacobian for formulations focusing on boundary conditions are provided in [9].

3.2. Local analysis of Jacobian . The asymptotic order of the inverse Jacobian can be evaluated locally. For general *systems* of nonlinear equations, the asymptotic order, m_J, $J^{-1}(Q) = O(h^{m_J})$ can be predicted by analyzing an *equivalent linear operator*, $E(Q)$. The equivalent linear operator is derived locally by a scaling analysis of the $J(Q)$ operator (3.6); the analysis evaluates magnitudes of the coefficients appearing in the matrix of the discrete Jacobian. In the scaling analysis, all discrete spatial derivatives operators contributing to the Jacobian are replaced with $O(1/h^k)$ terms, where k is the differentiation order. Surface integrals, i.e., terms like $\oint_\Gamma (g(Q)n_x)\, d\Gamma$, are replaced with $g(Q)O(h^{d-1})$ and volume integrals, i.e., terms like $\iint_\Omega g(Q)\, d\Omega$, are replaced with $g(Q)O(h^d)$; here $g(Q)$ is a functional of the (manufactured) solution and/or its derivatives and n_x is the x-directional component of the outward unit normal $\hat{n}$. We will refer to these replacements as *equivalent substitutions*. After equivalent substitutions, $E(Q)$ can be formally inverted to estimate the order of $J^{-1}(Q)$. For basic fluid equations, this analytical evaluation can be performed easily, as shown in subsequent examples.

Some simple practical rules can be suggested for quick evaluation of m_J for non-degenerate equations. A scalar (nonlinear) equation is called *non-degenerate* for a given manufactured solution, if the coefficients of the highest derivatives in the equation linearized around this solution do not all vanish; a system of differential equations is non-degenerate if the determinant of its linearization is non-degenerate. Note that change of variables does not affect equation degeneration; it is determined by the type of equation and the manufactured solution. With the chosen scaling factor (3.8), integration over dual-cell boundaries does not introduce an h-dependent factor to the Jacobian; control volume integration introduces a factor O(h).

For FVD schemes discretizing non-degenerate scalar conservation laws with zero source function S,

$$m_J = (\text{order of solution differentiation in } \mathbf{F}). \tag{3.10}$$

For example, for inviscid fluxes, $m_J = 0$; for viscous fluxes, $m_J = 1$. For system of equations, the operator $J^{-1}(Q)$ is a matrix, and the asymptotic order m_J may vary for different matrix entries. Examples of evaluation the asymptotic order for systems of equations are given subsequently for non-degenerate equations in Section 5.2.1 and for degenerate equations in Section 5.3 .

3.3. Error accumulation. The assessment of sources for possible error accumulation presented in this section follows the arguments provided in [10]. The discretization error can be considered as a convolution of the truncation-error function with the corresponding Green

function. Assuming that the Green function is smooth almost everywhere, there are two possible scenarios: (1) There is no significant truncation-error cancellation in the convolution integration. This scenario corresponds to global error accumulation and produces discretization errors converging with the same order as truncation errors. (2) There is a significant truncation-error cancellation in the convolution integration. In this case, locally produced errors dominate globally accumulated errors, and discretization errors converge with a higher order than truncation errors.

From (3.1), there are two contributors to the residual of an FVD scheme: flux computations and source/force computations. On irregular grids, the flux-related contributions do not cause dominant global discretization-error accumulation. The rationale is that a flux error at an internal face contributes equal and opposite amounts to the residuals on both sides of the face; thus, the generated error is (almost) canceled in the residual integration with a smooth convolution kernel. Some error accumulation may still occur because of variations in the convolution kernel, which is smooth, but not constant. On regular grids, this accumulated error might become dominant because the leading contributions to the local residuals are canceled out. The net result is that the discretization-error convergence order is expected to be the same on regular and irregular grids.

The source and force residual contributions at a control volume are independent of neighboring control volume residuals. Large smooth residual components can be introduced by the source/force integration method. To prevent accumulation of a dominant error, the integration method should provide a design-order accuracy for integration of a smooth function over any $O(1)$-large domain. Note that the local integration accuracy on individual control volumes is allowed to be lower order. An example is shown in Section 5.1.

3.4. Analysis of residual convergence. While residuals can be directly measured in computations, for scheme design purposes, it is useful to analyze separate factors contributing to the residual and determine the asymptotic residual order, m_R, $R(Q) = O(h^{m_R})$. The asymptotic order is evaluated for the chosen scaling factor (3.8).

3.4.1. Analysis of residual: flux contributions. There are three main flux-related contributors to $R(Q)$: (1) flux reconstruction, (2) dual-cell boundary approximation, and (3) flux integration; these contributions have also been identified in [18]. A pth-order residual $R(Q)$ ($m_R = p$) can be obtained, if the following three sufficient accuracy conditions are satisfied. The conditions are formulated in terms of the maximal degree of a polynomial, for which the considered approximation provides the exact outcome.

1. Flux reconstruction accuracy. The flux $\mathbf{F^h}$ should be reconstructed precisely at the control-volume boundaries for an analytical flux F represented by polynomials of the $(p-1)^{th}$ degree.

2. Control-volume boundary accuracy. The integral of the outward normal to the boundary should be computed precisely for each boundary segment (face) represented as a $(p-1)^{th}$-order curve, i.e., its (piecewise) parametric formulation with respect to the curve length involves only polynomials of the $(p-1)^{th}$ degree. In many practical cases, the control volumes in the interior have piecewise linear boundaries, so this contributor plays an important role only near the physical boundaries of the computational domain, where the imposed geometry must be approximated.

3. Flux integration accuracy. The flux integration method should be exact for fluxes represented as polynomials of the $(p-1)^{th}$ degree. Note that this condition relates to the accuracy of the integration scheme, and assumes no reconstruction errors. In particular, in 1D FVD schemes, this condition is satisfied for all polynomials because each of the two control-volume boundaries collapse to a single point. In multiple dimensions, one should

distinguish between the global and local integration accuracies. The *global* p^{th}-order integration accuracy is achieved when the numerical integration of polynomials of $(p-1)^{th}$ degree over the entire closed dual-cell boundary is exact, i.e., provides the same result as the analytical integration. To achieve the *local* integration accuracy of pth order, the $(p-1)^{th}$ degree polynomials should be integrated exactly over each segment (face) of the boundary. Local accuracy is more strict and implies global accuracy of the same order or higher; global p^{th}-order flux integration accuracy is sufficient. For many FVD schemes, local and global flux integration accuracies are the same; however, one commonly used FVD scheme discussed in Section 5.2.2 relies on an economic integration strategy that capitalizes on the global integration accuracy order exceeding the order of the local integration accuracy.

Each of these sufficient accuracy conditions can be evaluated separately and independently. Note: (1) the flux reconstruction and flux integration conditions recover the steps given in [4] for linear and quadratic schemes on unstructured meshes; (2) these conditions are conservative (not necessary) because higher-order approximation to $R(Q)$ can be achieved due to error cancellation, especially, on regular grids.

3.4.2. Analysis of residual: source and force contributions. Generally, to provide an $O(h^p)$ contribution to the residual $R(Q)$, it is sufficient for the numerical integration over the control volume to be exact for the integrated function represented by a polynomial of the $(p-2)^{th}$ degree. However, because of possible global error accumulation, this is not sufficient; the design p^{th}-order accuracy should be demonstrated in integration of an arbitrary smooth function over any $O(1)$-large domain. To verify an integration scheme, one can (1) choose a continuous function and integrate it analytically over an $O(1)$-large computational domain; (2) implement the studied numerical integration scheme over this domain on a sequence of globally refined meshes; and (3) monitor convergence of the integration error, which is expected to be $O(h^p)$, where p is the design order.

3.5. Error estimation and applications. The methodology for error estimation proposed in this paper suggests two ways to evaluate asymptotic convergence of truncation and discretization errors that would be observed in global grid-refinement computations on irregular grids.

The main computational analysis tool is a DS test that explicitly demonstrates error convergence which is used as predictor for the error convergence in global computations. The predictions of truncation-error convergence are always accurate, providing sufficient sampling of DS computational windows (i.e., if DS tests are performed in all representative locations). Predictions of discretization-error convergence may not be accurate on grids with increased regularity. DS tests are especially useful for scheme verification. Slow convergence of discretization errors detected in a DS test is an unambiguous indication of deficiency of the analyzed scheme.

Another, pure analytical, method is to use estimates for asymptotic orders of the inverse Jacobian and the residual. The analysis is especially useful for FVD scheme design because it identifies error contributions from separate parts of the scheme. For conservation laws with $J^{-1}(Q) = O(h^{m_J})$ and $R(Q) = O(h^{m_R})$, the truncation and discretization errors are evaluated from (3.9) and (3.7), respectively, as

$$E_t = O(h^{m_R-1}) \text{ and } E_d = O(h^{m_R+m_J}). \tag{3.11}$$

Both the DS tests and the estimates (3.11) should be complimented with a verification of the source/force integration scheme for global computations.

4. One-dimensional examples. Examples in this section show FVD schemes on one-dimensional (1D) irregular grids and illustrate applications of the analysis and DS tests to

predicting error convergence. For 1D equations, sufficient conditions for control-volume boundary accuracy and for flux-integration accuracy (conditions 2 and 3 in Section 3.4.1) are automatically satisfied. For simplicity, the examples considered in this section do not have source terms and the forcing term is integrated analytically, so m_R is fully determined by the flux reconstruction accuracy.

4.1. Discretization grids. A 1D discretization grid is defined as a combination of the primal and dual nodes. The solution values are located at the primal nodes; the fluxes are located at the dual nodes. For node-centered discretizations, a natural strategy is to place the primal mesh first and, then, use this mesh as a reference for placing dual control volumes.

The 1D node-centered discretization grids employed in this section are designed to study effects of grid irregularities and are described as follows. The first and the last of the $N + 1$ primal nodes, $x_i, i = 0, 1, \ldots, N$, are always located at the ends of the computational interval; the interior nodes can be distributed either uniformly or randomly. Either distribution retains the nodal ordering and ensures that the maximal distance between the neighboring nodes is $O(1/N)$. Let $s_i, i = 0, 1, \ldots, (N + 1)$ denote the flux locations. The first and the last fluxes are also located at the ends of the interval; the location of an interior flux, s_i, is always between the primal nodes x_{i-1} and x_i and initially defined as either a biased or an unbiased average; then, the dual node s_i may be randomly perturbed.

(a) Uniform primal mesh; unperturbed unbiased dual mesh

(b) Uniform primal mesh; perturbed unbiased dual mesh
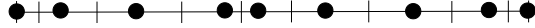
(c) Random primal mesh; unperturbed unbiased dual mesh

FIG. 4.1. *Examples of one-dimensional discretization grids: black bullets denote primal mesh nodes, vertical tic-marks denote dual mesh nodes*

Specifically, on an interval $x \in [a, b]$, the primal nodes are distributed according to

$$x_0 = a; \quad x_i = a + (i + r_i)\frac{b - a}{N}, \quad i = 1, \ldots, (N - 1); \quad x_N = b; \qquad (4.1)$$

where r_i is either zero (uniform primal mesh) or a random number $-0.4 \le r_i \le 0.4$ (random primal mesh). The dual-mesh nodes are computed accordingly as

$$s_0 = a; \quad s_i = x_{i-1} + d_i (x_i - x_{i-1}), \quad i = 1, \ldots, N; \quad s_{N+1} = b; \qquad (4.2)$$

where $d_i = 0.5$ corresponds to an unbiased unperturbed dual mesh; $d_i = 0.7$ corresponds to a biased unperturbed dual mesh; and $d_i = 0.5 + r_i^s$ or $d_i = 0.7 + r_i^s$ correspond to unbiased and

10

biased perturbed dual meshes, respectively; here r_i^s is a random number $-0.25 \le r_i^s \le 0.25$. Grid examples are shown in Figure 4.1. Note, that a combination of a random primal mesh and an unbiased, perturbed dual mesh is representative for multidimensional median-dual partition on irregular grids.

The global computations in this section refer to tests performed on the interval $x \in [0, 1]$ using a sequence of grids with the total number of grid nodes increasing as $N = 2^3, 2^4, \dots, 2^{14}$. The DS test is performed on a sequence of the intervals $[0.5 - l, \ 0.5 + l]$, where $l = 2^{-1}, 2^{-2}, \dots, 2^{-10}$ is a scaling factor; the random grids on each scale are generated independently; the number of grid nodes at each scale is fixed, $N = 16$.

4.2. Convection equation. In the first example concerned with a constant-coefficient convection equation, we illustrate applications of the DS test to predict the accuracy of irregular FVD schemes. The equation

$$\partial_x U = f(x), \quad U(0) = U_0 \tag{4.3}$$

is satisfied with the exact solution $U = \sin(x)$, $f = \cos(x)$. This is a constant-coefficient equation and, therefore, non-degenerate. FVD equations are formed as follows

$$F_{s_{i+1}} - F_{s_i} = \sin(s_{i+1}) - \sin(s_i), \quad i = 0, \dots, N. \tag{4.4}$$

The fluxes, F_{s_i}, approximate solution values at the flux locations, s_i, and are computed by fully-upwind extrapolations from the primal nodes (except for the first interior dual node) as

$$
\begin{aligned}
F_{s_0} &= U_0, \\
F_{s_1} &= \frac{(s_1 - x_0)U_1 + (x_1 - s_1)U_0}{x_1 - x_0}, \\
F_{s_i} &= \frac{(s_i - x_{i-2})U_{i-1} - (s_i - x_{i-1})U_{i-2}}{x_{i-1} - x_{i-2}}, \quad i = 2, \dots, N+1
\end{aligned}
\tag{4.5}
$$

where U_i is a discrete approximation to $U(x_i)$. These inviscid fluxes do not include solution derivatives and thus, according to (3.10), $J^{-1}(Q) = O(1)$ in all cases. All fluxes (4.5) are 2nd-order accurate and, thus, $R(Q) = O(h^2)$. The analysis predicts

$$E_d = O(h^2) \ \text{ and } \ E_t = O(h). \tag{4.6}$$

Figure 4.2 shows convergence rates obtained in grid-refinement and DS computations on irregular discretization grids involving random primal meshes and unbiased unperturbed dual meshes. The equivalent meshsize is taken as $h = \frac{1}{N}$, where N is the number of primal intervals in grid-refinement computations. The convergence history of the L_∞ and L_1 norms of truncation and discretization errors observed in the global computations confirms the sharp estimates obtained by the analysis (4.6) and in the DS tests.

Table 4.1 summarizes discretization and truncation error convergence rates observed in computations with 1D node-centered FVD schemes. Although not shown, similar convergence rates are observed for cell-centered FVD schemes. The results reveal two important trends valid for general non-degenerate inviscid equations: (1) grid irregularity strongly affects the truncation-error convergence, but has no effect on convergence of the discretization errors; (2) bias does not affect convergence rates. The analysis estimates are sharp for discretization errors on all grids and for truncation errors on all "randomized" grids. The convergence of truncation errors on uniform unperturbed grids is 2nd order because of error cancellations occurring on these regular grids. The DS-test convergence rates accurately predict the corresponding rates observed in global computations on all grids. Note that in multidimensional computations on regular grids, DS tests usually overestimate convergence of discretization errors.

11
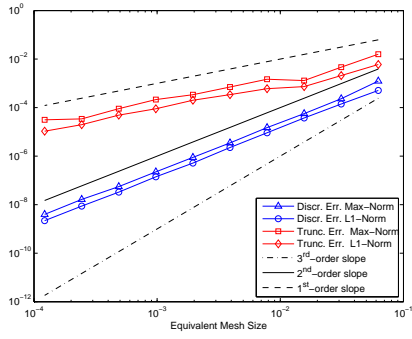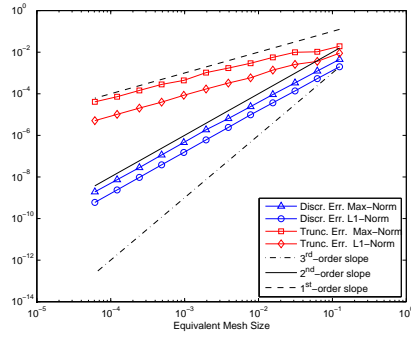
(a) DS test   (b) Grid refinement computations

FIG. 4.2. *Convergence of discretization and truncation errors in the DS test (a) and in grid-refinement computations (b) for the constant-coefficient convection equation. The tests are performed with random primal meshes and unbiased unperturbed dual meshes.*

Primal	Dual	DS test		Grid-refinement computations	
Mesh	Mesh	Discr. Error	Trunc. Error	Discr. Error	Trunc. Error
Uniform	Unbiased, Unperturbed	$O(h^2)$	$O(h^2)$	$O(h^2)$	$O(h^2)$
Uniform	Biased, Unperturbed	$O(h^2)$	$O(h^2)$	$O(h^2)$	$O(h^2)$
Uniform	Unbiased Perturbed	$O(h^2)$	$O(h)$	$O(h^2)$	$O(h)$
Uniform	Biased Perturbed	$O(h^2)$	$O(h)$	$O(h^2)$	$O(h)$
Random	Unbiased, Unperturbed	$O(h^2)$	$O(h)$	$O(h^2)$	$O(h)$
Random	Biased, Unperturbed	$O(h^2)$	$O(h)$	$O(h^2)$	$O(h)$
Random	Unbiased, Perturbed	$O(h^2)$	$O(h)$	$O(h^2)$	$O(h)$
Random	Biased, Perturbed	$O(h^2)$	$O(h)$	$O(h^2)$	$O(h)$

TABLE 4.1

Convergence of discretization and truncation errors for node-centered FVD schemes for the constant-coefficient convection equation.

4.3. Diffusion equation. The second set of one-dimensional tests illustrates the application of the DS analysis methodology to the diffusion equation. The non-degenerate constant-coefficient equation

$$\partial_{xx} U = f(x), \quad U(0) = \bar{U}_0, \quad U(1) = \bar{U}_1, \tag{4.7}$$

is defined on the interval $x \in [0, \ 1]$, with the exact solution $U = \sin(x)$, $f = -\sin(x)$. FVD equations are formed as

$$F_{s_{i+1}} - F_{s_i} = \cos(s_{i+1}) - \cos(s_i), \quad i = 1, \dots, N; \quad U_0 = \bar{U}_0; \quad U_N = \bar{U}_1. \tag{4.8}$$

12

Fluxes approximating the solution derivative are defined as

$$F_{s_i} = \frac{U_i - U_{i-1}}{x_i - x_{i-1}}, \quad i = 1, \ldots, N, \tag{4.9}$$

where U_i is a discrete approximation to $U(x_i)$. Dirichlet boundary conditions are enforced. According to (3.10), $J^{-1}(Q) = O(h)$.

Primal Mesh	Dual Mesh	DS test		Grid-refinement computations	
		Discr. Error	Trunc. Error	Discr. Error	Trunc. Error
Uniform	Unbiased, Unperturbed	$O(h^4)$	$O(h^2)$	$O(h^2)$	$O(h^2)$
Uniform	Biased, Unperturbed	$O(h^3)$	$O(h)$	$O(h)$	$O(h)$
Uniform	Unbiased, Perturbed	$O(h^2)$	$O(1)$	$O(h^2)$	$O(1)$
Uniform	Biased, Perturbed	$O(h^2)$	$O(1)$	$O(h)$	$O(1)$
Random	Unbiased, Unperturbed	$O(h^3)$	$O(h)$	$O(h^2)$	$O(h)$
Random	Biased, Unperturbed	$O(h^2)$	$O(1)$	$O(h)$	$O(1)$
Random	Unbiased, Perturbed	$O(h^2)$	$O(1)$	$O(h^2)$	$O(1)$
Random	Biased, Perturbed	$O(h^2)$	$O(1)$	$O(h)$	$O(1)$

TABLE 4.2

Convergence of discretization and truncation errors for node-centered FVD schemes for the diffusion equation. The analytical estimates accurately predict DS-test convergence rates for all grid types except uniform-primal/unperturbed-dual type. The DS tests accurately predict convergence orders of grid-refinement truncation errors. The discretization-error convergence order is predicted well for the unbiased perturbed dual meshes, but overestimated in other cases.

The placement of dual nodes (flux locations) significantly affects the error convergence. For unbiased, unperturbed dual meshes, the fluxes are approximated with the 2nd-order accuracy, thus, providing $R(Q) = O(h^2)$; for such FVD schemes, the analysis predicts

$$E_d = O(h^3) \text{ and } E_t = O(h). \tag{4.10}$$

For either perturbed or biased dual meshes, $R(Q) = O(h)$, and the corresponding estimates are

$$E_d = O(h^2) \text{ and } E_t = O(1). \tag{4.11}$$

Table 4.2 summarizes the discretization and truncation error convergence rates observed for 1D node-centered FVD schemes. The two main observations about grid-refined convergence rates of discretization errors are (1) local "random" grid irregularities do not affect the discretization-error convergence and (2) grid bias leads to one-order convergence deterioration.

The analytical estimates (4.10) and (4.11) accurately predict DS-test convergence rates for all grid types except uniform-primal/unperturbed-dual type; the convergence rates on these regular grids are faster because of local error cancellation. The DS tests accurately predict convergence orders of grid-refinement truncation errors. The discretization-error convergence order is predicted well for the unbiased perturbed dual meshes, but overestimated

13

in other cases. The reason for this overestimation is the error accumulation occurring in grid-refinement computations for all dual meshes except the unbiased perturbed type. Based on experience to date, in multidimensional computations on general irregular grids, the estimates obtained by the analysis and in DS tests are sharp as shown in following sections.
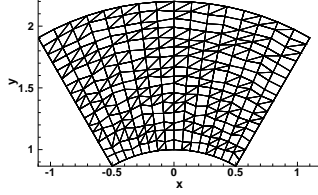
5. Two-dimensional computations.

FIG. 5.1. *A typical mixed-element unstructured grid generated with random splitting and random perturbation of the underlying quadrilateral grid.*

5.1. Poisson equation. As a two-dimensional scalar example, we solve the Poisson equation,

$$\Delta U = f, \tag{5.1}$$

with Dirichlet boundary conditions, on a series of primal mixed-element grids composed of triangles and quadrangles. Each grid is formed from an underlying regular quadrilateral grid (Figure 5.1). In terms of a polar, (r, θ), coordinate system, the grid extent is defined as $\theta \in [\pi/6, \pi/3]$ in the circumferential direction and $r \in [1, 2.2]$ in the radial direction. Grid irregularity is enforced by random splitting (or not splitting) quadrangles into triangles; approximately half of the quadrangles are split. In addition, the interior grid points are perturbed from their original position by random shifts in the range $[-\sqrt{2}/6, \sqrt{2}/6]$ of the local mesh size in the radial direction.
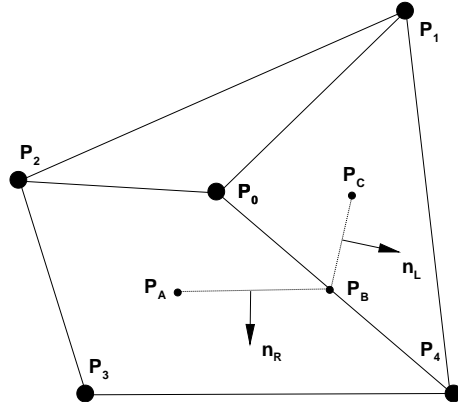

FIG. 5.2. *Illustration of gradient reconstruction for viscous terms on mixed grids with median-dual partition.*

The exact solution and forcing term are taken as $U = [(\sin(\pi x))^2 + (\sin(\pi y))^2]/2$, $f = -2\pi^2[1 - (\cos(\pi x))^2 - (\cos(\pi y))^2]$. In the FVD scheme, the solution is represented as a piecewise polynomial function, with polynomials defined at the primal cells; the conservation

14

law

$$\oint_{\Gamma} \nabla \mathbf{U} \cdot \hat{\mathbf{n}} \, d\Gamma = \iint_{\Omega} f \, d\Omega \qquad (5.2)$$

is enforced on node-centered control volumes constructed by the median-dual partition.

With reference to Figure 5.2, the integral flux through the dual faces adjacent to the edge $[P_0, P_4]$ is computed as

$$\int_{ABC} \nabla \mathbf{U} \cdot \hat{\mathbf{n}} \, d\Gamma = \nabla \mathbf{U}^R \cdot \mathbf{n_R} + \nabla \mathbf{U}^L \cdot \mathbf{n_L}, \qquad (5.3)$$

where $\mathbf{n_R}$ and $\mathbf{n_L}$ are directed areas of the corresponding dual faces. The gradient is reconstructed separately at each dual face as follows.

For the triangular element contribution, the gradient is determined from a Green-Gauss evaluation at the primal-grid element,

$$\nabla \mathbf{U}^L = \overline{\nabla \mathbf{U}}_{014}. \qquad (5.4)$$

The gradient overbar denotes a gradient evaluated by the Green-Gauss formula on the primal cell identified by the point subscripts. With fully-triangular elements, the formulation is equivalent to a Galerkin finite element scheme with a linear basis function [2, 3]. For the quadrilateral element contribution, the gradient is evaluated as

$$\nabla \mathbf{U}^R = \overline{\nabla \mathbf{U}}_{0234} + \left[\frac{U_4 - U_0}{|\mathbf{r}_4 - \mathbf{r}_0|} - \overline{\nabla \mathbf{U}}_{0234} \cdot \mathbf{e}_{04} \right] \mathbf{e}_{04}, \qquad (5.5)$$

where $\mathbf{r}_i$ is the coordinate vector of node P_i and

$$\mathbf{e}_{04} = \frac{\mathbf{r}_4 - \mathbf{r}_0}{|\mathbf{r}_4 - \mathbf{r}_0|} \qquad (5.6)$$

is the unit vector aligned with the edge $[P_0, P_4]$. Note that for grids with dual faces perpendicular to the edges, the edge-gradient is the only contributor. This approach to the gradient reconstruction is used to decrease the scheme susceptibility to odd-even decoupling [11, 12]. In all cases, the linear solution reconstruction leads to the 1st-order flux (gradient) reconstruction accuracy.

The sequences of globally refined grids are generated with $2^{n+3} + 1$ points in both the radial and circumferential directions, where $n = 0, 1, 2, 3, 4$. The volume integral of the forcing term in (5.2) is evaluated as the value at the node multiplied by the dual volume. This integration is first order locally, but second-order convergence of this integration method over any $O(1)$ domain is observed on general mixed-element grids. The sequences of DS grids are generated from a grid with 17 points in both the nominal radial and circumferential directions and downscaled by the scaled-grid method about the center of the domain by a factor 2^{-s}, where $s = 0, 2, 4, 6, 8$. The grid topology remains unchanged.

The asymptotic order of $J^{-1}(Q)$, computed according to (3.10), is $m_J = 1$. Overall, $R(Q) = O(h)$ and the analysis predicts

$$E_d = O(h^2) \text{ and } E_t = O(1). \qquad (5.7)$$

The L_1 norms of truncation and discretization errors are shown in Figure 5.3 versus an equivalent mesh size parameter, taken as the L_1 norm of the square root of the dual volume.

15

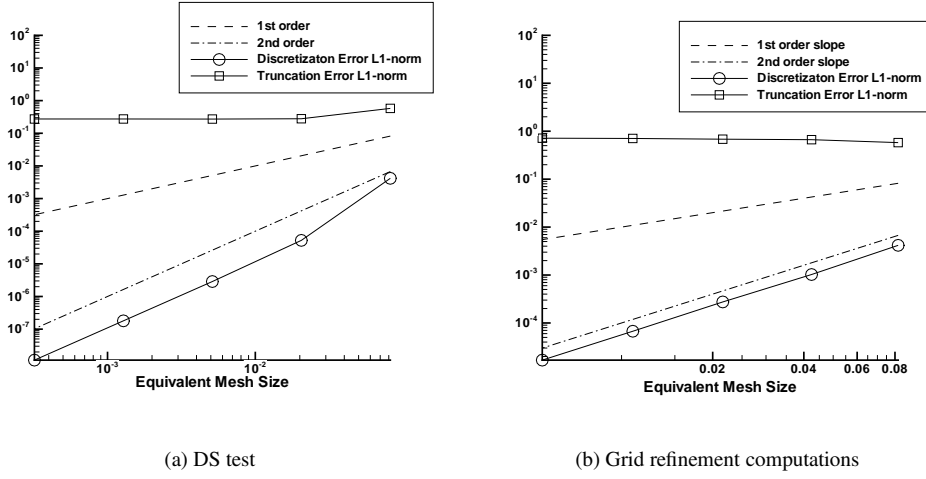|	
(a) DS test	(b) Grid refinement computations

FIG. 5.3. *Convergence of the discretization and truncation errors for the Poisson equation solved on mixed-element unstructured grids.*

Although not shown, error convergence rates in the L_∞ norm are the same as the L_1-norm rates. The analysis (5.7) and the DS tests predict grid-refinement error convergence rate precisely; the truncation errors remain $O(1)$ and the discretization errors converge with 2nd-order. The reason for the $O(1)$ convergence of truncation errors is grid irregularity stemming from the perturbation to the grid points and the usage of mixed grids. Both references [19] and [22] interpret $O(1)$ convergence of truncation errors on irregular grids as indication that the corresponding discrete solutions do not approximate the continuous ones; this example clearly shows that this is not the case. Although not shown, with regular meshes composed of either triangles alone or quadrangles alone, both the truncation errors and the discretization errors converge with 2nd order.

5.2. Incompressible Euler equations. In this section we consider incompressible inviscid flow equations. The source function S is assumed to be zero. Inviscid fluxes for conservation of mass and momentum are defined as

$$\mathbf{F} = \mathbf{f}\bar{\mathbf{i}} + \mathbf{g}\bar{\mathbf{j}} = \begin{bmatrix} \bar{\beta}u \\ u^2 + p \\ uv \end{bmatrix} \bar{\mathbf{i}} + \begin{bmatrix} \bar{\beta}v \\ uv \\ v^2 + p \end{bmatrix} \bar{\mathbf{j}}, \tag{5.8}$$

where the vector of unknowns, $q = [u, v, p]$, includes the Cartesian velocities and the pressure; β is an artificial compressibility parameter introduced as in [2] and taken as $\bar{\beta} = 1$ here.

The median-dual partition is applied. At each dual control volume, a polynomial solution approximation is constructed. The approximation is required to coincide with the discrete solution value at the central node P_0; the polynomial coefficients are determined through a least-square procedure involving neighboring nodes, i.e., nodes linked by an edge to the central node P_0. If the set of neighboring nodes is insufficient to determine, uniquely and stably, the polynomial coefficients, the set may be expanded to involve neighbors of neighbors. Three node-centered FVD schemes are considered: an edge-reconstruction scheme and two face-reconstruction schemes.

16

5.2.1. Equivalent linear operator analysis. The Jacobian of $\oint_\Gamma (\mathbf{F} \cdot \hat{\mathbf{n}}) \, d\Gamma$ is a 3×3 matrix

$$\oint_\Gamma \begin{pmatrix} n_x & n_y & 0 \\ 2un_x + vn_y & un_y & n_x \\ vn_x & un_x + 2vn_y & n_y \end{pmatrix} d\Gamma \tag{5.9}$$

operating on the vector $\delta q = [\delta u, \delta v, \delta p]^T$. After equivalent substitutions, the equivalent linear operator, $E(Q)$, becomes

$$E(Q) = \begin{pmatrix} O(1) & O(1) & 0 \\ uO(1) + vO(1) & uO(1) & O(1) \\ vO(1) & uO(1) + vO(1) & O(1) \end{pmatrix}. \tag{5.10}$$

If $u^2 + v^2 > \varepsilon > 0$ everywhere in the computational domain, i.e., the system is non-degenerate, the inverse of $E(Q)$ is a full matrix

$$J^{-1}(Q) \sim E^{-1}(Q) = \begin{pmatrix} O(1) & O(1) & O(1) \\ O(1) & O(1) & O(1) \\ O(1) & O(1) & O(1) \end{pmatrix}. \tag{5.11}$$

Thus, the estimate of the discretization error convergence is fully determined by convergence of contributors to the residual $R(Q)$ (Section 3.4.1). In a general situation, the asymptotic order of $J^{-1}(Q)$ can be different for different equations, but for non-degenerate (away from stagnation) inviscid flow equations, the asymptotic order is $m_J = 0$ for all three equations. The effect of degeneration (flow stagnation) on convergence of the discretization errors is considered subsequently in Section 5.3. In the course of Section 5.2, we assume non-degenerate equations implying non-vanishing velocity components of the (manufactured) solution.
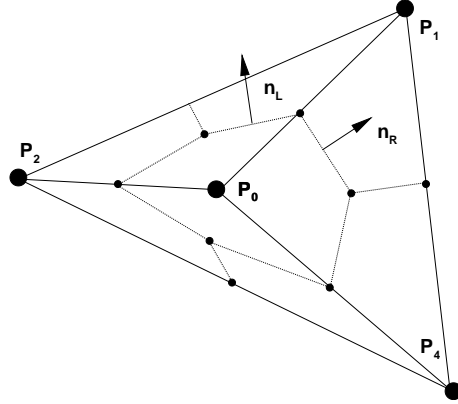

FIG. 5.4. *Illustration for edge-reconstruction flux integration scheme in the interior.*

5.2.2. Edge-reconstruction scheme. This edge-reconstruction FVD scheme is widely used in unstructured-grid computations [2, 3, 11, 12, 19]. The term edge-reconstruction emphasizes that the quadrature scheme used for computing the integrals over the dual-cell boundaries employs fluxes reconstructed at the midpoints of the edges connecting the grid

17

nodes. By construction, the dual-cell boundaries are piecewise linear and, therefore, in the interior and next to straight physical boundaries, the outward normal $\hat{\mathbf{n}}$ approximation is exact.

The numerical upwind flux at the edge midpoint is approximated according to the Roe scheme [2, 21],

$$\left(\mathbf{F^h} \cdot \hat{\mathbf{n}}\right) = \frac{1}{2}\left[(\mathbf{F_0} \cdot \hat{\mathbf{n}}) + (\mathbf{F_1} \cdot \hat{\mathbf{n}})\right] - \frac{1}{2}\left|\mathbf{A}(\bar{\mathbf{Q}})\right|(\mathbf{Q_1} - \mathbf{Q_0}), \qquad (5.12)$$

where, $\mathbf{Q_0}$ and $\mathbf{Q_1}$ are the "left" and "right" solution reconstructions at the edge midpoint derived from the linear approximations at the control volumes centered at P_0 and P_1, respectively (see Figure 5.4); $\mathbf{F_0}$ and $\mathbf{F_1}$ are the corresponding "left" and "right" numerical fluxes; $\hat{\mathbf{n}}$ is the unit vector aligned with the combined-directed-area vector $\mathbf{n} = \mathbf{n_L} + \mathbf{n_R}$, where $\mathbf{n_L}$ and $\mathbf{n_R}$ are outward normal (directed-area) vectors of the left and right segments, respectively, with their lengths equal to the corresponding segment lengths; $\left|\mathbf{A}(\bar{\mathbf{Q}})\right|$ is the Roe's approximate Riemann solver matrix computed for $\bar{\mathbf{Q}} = \frac{1}{2}(\mathbf{Q_1} + \mathbf{Q_0})$. With a linear solution approximation at each control volume, this is a 2nd-order accurate flux reconstruction.

The flux integration over the two segments of the control-volume boundary linked at the edge midpoint is approximated by multiplying $\mathbf{F^h}$ computed at the edge midpoint with the length of the combined-directed-area vector, $|\mathbf{n}|$. This computationally efficient scheme provides exact integration for the conservation laws with linear fluxes on triangular grids, where it corresponds to a linear finite-element Galerkin scheme [2, 3, 4]. According to the definition introduced in the sufficient flux-integration accuracy (condition 3 in Section 3.4.1), the scheme possesses global 2nd-order accuracy, The scheme provides only 1st-order local integration accuracy. On general (irregular) quadrilateral and mixed-element grids, the global flux integration accuracy deteriorates to 1st order; examples are shown subsequently in Section 5.2.4; additional examples can be found in [8].

The forcing term integration over the control volume is approximated as the node value multiplied by the volume $|\Omega|$. This integration method is first-order accurate locally, but the integration over any $O(1)$ domain is second order on general globally refined grids with a median-dual partition. Boundary conditions are enforced weakly through the boundary fluxes; implementation details are given in Appendix A. The overall residual convergence is the same for all equations and is estimated as $R(Q) = O(h^2)$ on triangular grids and $R(Q) = O(h)$ on general quadrilateral and mixed-element grids, leading to estimates

$$E_d = O(h^2) \text{ and } E_t = O(h) \qquad (5.13)$$

for irregular triangular grids and

$$E_d = O(h) \text{ and } E_t = O(1) \qquad (5.14)$$

for general irregular grids.

5.2.3. Face-reconstruction schemes. In this section, we describe two face-reconstruction FVD schemes that employ the median-dual partition, and provide 2nd and 3rd order accuracies on general irregular grids. The term face-reconstruction refers to the Gauss-Legendre method for flux integration; the method uses fluxes reconstructed at Gaussian points defined at each segment (face) of the dual-cell boundaries. Similar to the edge-reconstruction scheme, the linear and quadratic polynomials are defined at dual cells and coincide with the solutions at the grid nodes. The polynomial coefficients are defined in a least-square procedure involving solutions at the neighboring nodes. In the interior, piecewise-straight dual boundaries imply an exact $\hat{\mathbf{n}}$. The schemes described in this section are quite similar to the scheme discussed by Delanaye and Liu [6] for cell-centered discretizations. As noted therein and shown

in [8], the operation counts significantly favor the cell-centered approach for flux integration in three dimensions.

The distinguishing feature of these face-reconstruction schemes is the flux integration procedures ensuring the designed *local* integration accuracy. Extension of 2nd-order accuracy to mixed grids can be achieved with linear polynomials, a modified straight-segment tangency boundary approximation (discussed subsequently in Section 5.2.4), and a flux integration scheme providing local 2nd-order accuracy. Accuracy of 3rd order requires quadratic polynomials for flux reconstruction, quadratic fit to the curved tangency boundary, and an flux integration scheme with local 3rd-order accuracy.

In the implemented 2D version, a polynomial flux is defined at each segment of the dual control-volume boundary and used in (5.12). The "left" and "right" solutions, $\mathbf{Q_0}$ and $\mathbf{Q_1}$, are represented by the basic polynomials defined at the adjacent control volumes; numerical fluxes, $\mathbf{F_0}$ and $\mathbf{F_1}$, are analytically computed as products of the corresponding basic polynomials. The dissipation matrix, $\left|\mathbf{A}(\bar{\mathbf{Q}})\right|$, is computed for $\bar{\mathbf{Q}}$, defined as the average of $\mathbf{Q_0}$ and $\mathbf{Q_1}$ evaluated at the segment midpoint. The polynomial flux at this segment is defined according to (5.12), where all terms, beside $\left|\mathbf{A}(\bar{\mathbf{Q}})\right|$, are polynomials. The scheme with linear polynomials provides 2nd-order accurate flux reconstruction; fluxes reconstructed with quadratic polynomials are 3rd-order accurate.

The inner product of the polynomial flux vector and the outward unit normal vector is integrated over each segment of the dual-cell boundary with a numerical Gauss-Legendre quadrature formula employing 1 point for the linear face-reconstruction scheme, and 2 points for the quadratic face-reconstruction scheme. As a convenient debugging tool, one can add one Gaussian point to have total of 2 and 3 points, respectively, per integration segment. With these improved accuracy integrations, the FVD method should provide zero residuals for linear and quadratic manufactured solutions.

The forcing term integration method for the linear face-reconstruction scheme is the same as for the edge-reconstruction scheme, providing 2nd-order accuracy. For quadratic face-reconstruction scheme, a linear (or piecewise linear) approximation to the forcing term is constructed and integrated at each control volume providing a 3rd-order accurate approximation to $\frac{1}{|\Gamma|} \iint_{\Omega} f \, d\Omega$. Description of boundary condition implementation for the face-reconstruction FVD schemes is provided in Appendix A. Overall, $R(Q) = O(h^2)$ for the linear scheme and $R(Q) = O(h^3)$ for the quadratic scheme; residual convergence does not deteriorate for general irregular grids. The predictions for the error convergence rates are

$$E_d = O(h^2) \ \text{ and } \ E_t = O(h) \tag{5.15}$$

for the linear FVD scheme and

$$E_d = O(h^3) \ \text{ and } \ E_t = O(h^2) \tag{5.16}$$

for the quadratic FVD scheme.

5.2.4. Numerical tests for non-degenerate flows. Numerical tests presented in this section are performed for 2D inviscid incompressible flows around a cylinder of unit radius centered in the origin. The flow is described by the conservative equations (1.1) with zero source and forcing terms and fluxes defined in (5.8). The analytical solution for this problem is known

$$
\begin{aligned}
U &= U_\infty + \tfrac{2\sin^2\theta - 1}{r^2} + \partial_y \psi, \\
V &= V_\infty + 2\tfrac{\sin\theta\cos\theta}{r^2} - \partial_x \psi, \\
P &= P_\infty - \tfrac{U^2 + V^2}{2},
\end{aligned}
\tag{5.17}
$$

where (r, θ) are the polar coordinates $r^2 = x^2 + y^2$, $\tan\theta = y/x$, and $\psi = -C\ln(r)$ is the stream function with C being a constant characterizing the flow circulation. In the course of this section, the free stream at the infinity is characterized by $U_\infty = 1$, $V_\infty = 0$, $P_\infty = 1.5$, and the zero circulation ($C = 0$) is assumed.
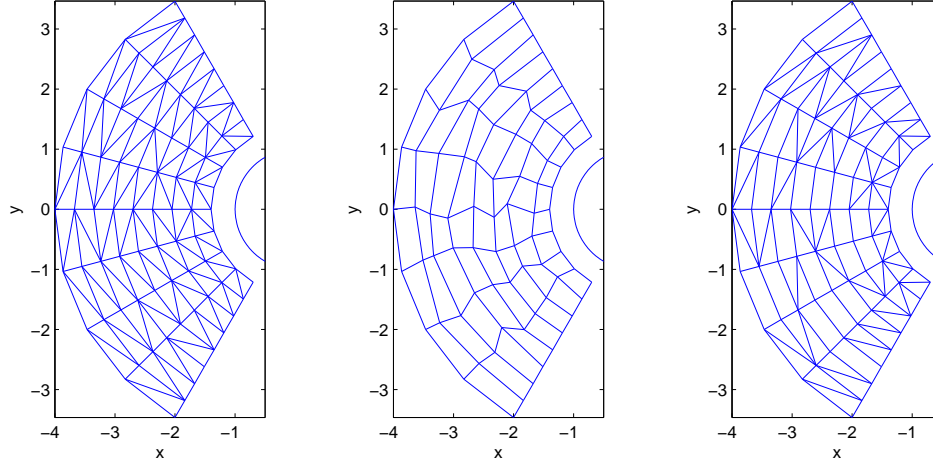
(a) Irregular triangular grid   (b) Irregular quadrilateral grid   (c) Irregular mixed grid

FIG. 5.5. *Typical triangular and mixed-element unstructured grids defined on a computational domain shifted away from the surface of the cylinder.*

Interior inflow/outflow domains. The first set of tests is performed on a computational domain shifted away from the surface of the cylinder: $1.5 \leq r \leq 4$, $2\pi/3 \leq \theta \leq 4\pi/3$. Seven formulations are studied: the edge-reconstruction FVD scheme on irregular triangular, quadrilateral, and mixed-element grids; and face-reconstruction FVD schemes on irregular quadrilateral and mixed-element grids. Examples of irregular grids derived from an underlying regular grid are shown in Figure 5.5. For triangular and mixed-element grids, irregularity is introduced through random splitting (or not splitting) of structured quadrilateral cells. Each cell has equal probabilities to introduce either of the two diagonal choices or, for mixed-element grids, no diagonals. For irregular quadrilateral grids, interior nodes are perturbed from their original position by random shifts in the range $[-\sqrt{2}/6, \sqrt{2}/6]$ of the local mesh size in both the radial and circumferential directions.

For each formulation, grid refinement and DS tests are performed. In grid refinements, the underlined regular grid is refined by doubling the number of intervals in the radial and angular directions. In the DS test, the coarsest 9×9 grid is scaled down around the point $r = 2.75$, $\theta = \pi$ by multiplying all angular and radial deviations from this point by a factor of 0.5. Randomization is introduced independently on each scale. The inflow boundary conditions are enforced at the boundary corresponding to the external radius; outflow conditions are enforced at all other boundaries. Table 5.1 summarizes the convergence of discretization and truncation errors observed in these tests. The results confirm the analytical predictions (5.13) — (5.16) and the capabilities of the DS test to provide sharp estimates for error convergence in grid-refinement computations.

The convergence rates observed for the edge-reconstruction scheme on irregular triangu-

Formulation	Analysis / DS test		Grid-refinement computations	
	Discr. Error	Trunc. Error	Discr. Error	Trunc. Error
Edge-reconstruction, irregular triangular grid	$O(h^2)$	$O(h)$	$O(h^2)$	$O(h)$
Edge-reconstruction, irregular quadrilateral grid	$O(h)$	$O(1)$	$O(h)$	$O(1)$
Edge-reconstruction, mixed-element grid	$O(h)$	$O(1)$	$O(h)$	$O(1)$
Linear face-reconstruction, irregular quadrilateral grid	$O(h^2)$	$O(h)$	$O(h^2)$	$O(h)$
Linear face-reconstruction, mixed-element grid	$O(h^2)$	$O(h)$	$O(h^2)$	$O(h)$
Quadratic face-reconstruction, irregular quadrilateral grid	$O(h^3)$	$O(h^2)$	$O(h^3)$	$O(h^2)$
Quadratic face-reconstruction, mixed-element grid	$O(h^3)$	$O(h^2)$	$O(h^3)$	$O(h^2)$

TABLE 5.1

Convergence of discretization and truncation errors for various irregular grid formulation of the 2D inviscid incompressible equations on an inflow/outflow computational domain. The error convergence orders predicted by the analysis are observed for all variables and equations in all norms.

lar and irregular quadrilateral grids are consistent with the results reported in [1]. Although not shown, we have implemented a central version of the edge-reconstruction scheme, where fluxes at the edge midpoints are defined as averages of the solutions in the neighboring nodes The observed convergence rates were identical with the rates shown in Table 5.1. The results contradict to [19], where zeroth-order convergence of discretization errors on irregular quadrilateral grids was reported for a central scheme for a constant-coefficient convection equation. An in-depth investigation of this discrepancy confirming correctness of our results has been reported in [8].

Tangency boundary. For the edge-reconstruction FVD scheme on triangular grids, local accuracy deterioration occurs if a curved tangency boundary is approximated by straight segments linking primal-mesh nodes located at the physical boundary. Sketch (a) of Figure 5.6 illustrates this approximation: the straight segments $[P_2, P_0]$ and $[P_0, P_4]$ approximate a curved boundary, the points P_B and P_C are the segments' midpoints, and the arrow indicates the local flow velocity. For the edge-reconstruction scheme, discrete tangency is enforced over the straight segments $[P_0, P_B]$ and $[P_0, P_C]$. The exact continuous solution satisfies the tangency condition at the actual curved boundary, not at the straight boundary segments. If evaluated with the exact solution, one boundary segment would appear as inflow, while the other would appear as outflow.

To assess the error introduced by implementing zero velocities over the straight boundary segments, consider the segment $[P_B, P_0]$ that contributes to the control volume centered at P_0. An overspecified version of the boundary conditions, in which the exact velocities are reconstructed at $\bar{P} = 5/6P_0 + 1/6P_2$, would complement the interior edge-reconstruction formulation to provide a 2nd-order accurate solution [3]. Thus, the difference between this overspecified boundary flux and the weak tangency boundary condition can be considered
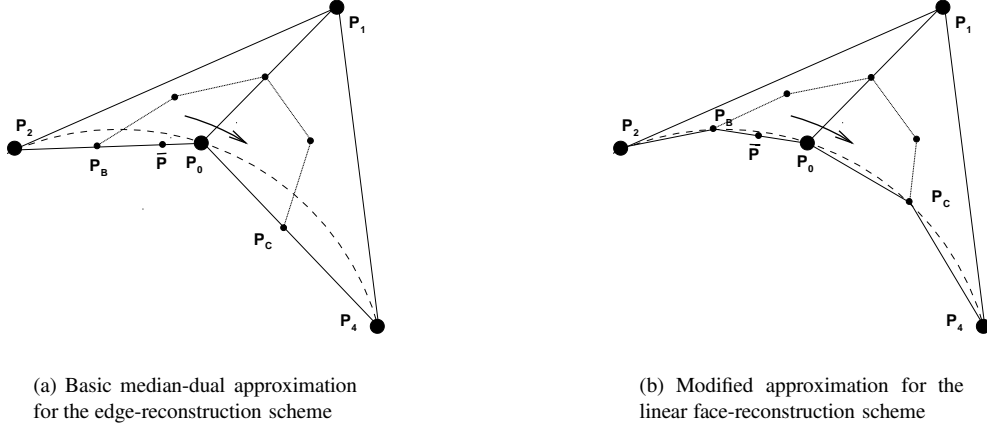
21

(a) Basic median-dual approximation
for the edge-reconstruction scheme

(b) Modified approximation for the
linear face-reconstruction scheme

FIG. 5.6. *Straight-segment approximations to curved tangency boundary.*

as a velocity reconstruction error. In particular, for the mass conservation law, the leading
contribution to $R(Q)$ from the segment $[P_0, P_B]$ can be estimated as

$$R_{[P_B,P_0]} = \bar{\mathbf{V}} \cdot \bar{\mathbf{n}} = O(h), \qquad (5.18)$$

where

$$\bar{\mathbf{V}} = \tfrac{5}{6}\mathbf{V}_0 + \tfrac{1}{6}\mathbf{V}_2 = \tfrac{1}{2}\left(\mathbf{V}_0 + \mathbf{V}_2\right) + O(h),$$
$$\bar{\mathbf{n}} = \tfrac{1}{2}\left(\hat{\mathbf{n}}_0 + \hat{\mathbf{n}}_2\right) + O(h^2).$$

and

$$(\mathbf{V}_0 + \mathbf{V}_2) \cdot (\hat{\mathbf{n}}_0 + \hat{\mathbf{n}}_2) = O(h^2),$$

Here, $\bar{\mathbf{V}}$ is the velocity vector reconstructed at $\bar{P}$ and $\bar{\mathbf{n}}$ is the outward unit normal corresponding to $[P_0, P_B]$, $\mathbf{V}_0$, $\hat{\mathbf{n}}_0$, $\mathbf{V}_2$, $\hat{\mathbf{n}}_2$, are the exact velocities and unit normals at the grid nodes P_0 and P_2, respectively, satisfying $(\mathbf{V}_0 \cdot \hat{\mathbf{n}}_0) = (\mathbf{V}_2 \cdot \hat{\mathbf{n}}_2) = 0$, and h is the characteristic meshsize. The 1st-order accuracy in $R(Q)$ leads to local 1st-order accurate discretization errors. The reason for the residual contribution, $R_{[P_B,P_0]}$, to be $O(h)$ is the 1st-order difference between $\bar{\mathbf{V}}$ and $(\mathbf{V}_0 + \mathbf{V}_2)/2$. Similar $O(h)$ contributions appear in momentum-conservation equations.

To illustrate the effect of a straight-segment approximation to a curved tangency boundary, a sequence of irregular triangular grids is generated at the top of the cylinder ($1 \leq r \leq 2.2$, $\pi/3 \leq \theta \leq 2\pi/3$) and used in computations with the edge-reconstruction FVD scheme; a grid example is shown in Figure 5.7. Figure 5.8 illustrates convergence of the L_1 norm of truncation and discretization errors in grid-refinement and DS tests performed with edge-reconstruction FVD scheme. Two DS tests are performed, each with the focal point at the top surface of the cylinder. The first DS test uses overspecification at all boundaries except the interior tangency nodes. The second DS test replaces the overspecification along one boundary with the physical inflow boundary condition (see sketches in Figure 5.8).

For the interior-tangency nodes, there are two tangency segments; the errors at these segments contribute to $R(Q)$ with opposite signs and, at least partially, compensate each other. Because of this compensation, the accuracy deterioration does not affect interior-tangency nodes on the grids with (nearly) uniform boundary node distributions. The 2nd-order convergence of discretization errors and the 1st-order convergence of truncation errors demonstrated
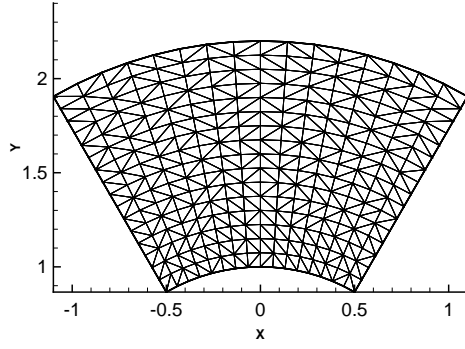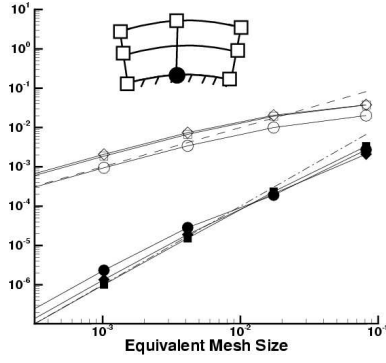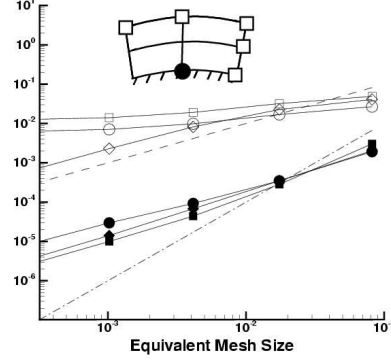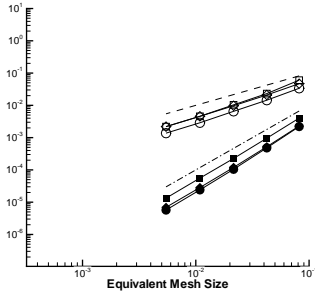
22

FIG. 5.7. *Irregular triangular grid around the top of the cylinder.*

(a) DS test: interior tangency boundary conditions

(b) DS test: inflow/tangency boundary conditions
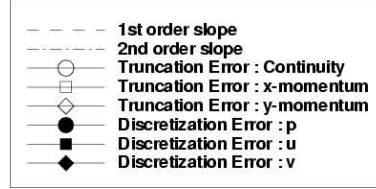

(c) Grid refinement

FIG. 5.8. *Convergence of the L_1 norm of truncation and discretization errors observed in DS and grid-refinement tests for the edge-reconstruction FVD scheme. The tests are performed on irregular triangular grids surrounding the top tangency boundary of the unit cylinder. The open square symbols in the sketches denote over-specification for the DS tests.*

23

in the interior-tangency DS test confirm this conclusion. However, in the corners or/and at the interfaces between clusters of boundary nodes with different topology/metrics, the compensation does not occur. The accuracy deterioration is clearly observed in the DS test performed with the inflow/tangency boundary conditions. The convergence of the L_1 norms of the errors in the grid-refinement test is the same as convergence shown in the interior-tangency DS test and is not affected by local accuracy deterioration in the corners; although not shown, the grid-refinement convergence of the L_∞ norm of errors is slower and similar to the convergence demonstrated in the DS test with the inflow/tangency boundary conditions.

(a) DS test: basic approximation   (b) DS test: modified approximation

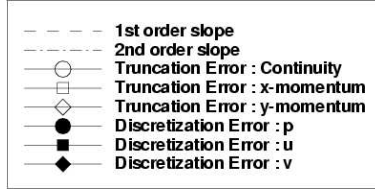|	
– – – –	1st order slope
– · – · –	2nd order slope
—◯—	Truncation Error : Continuity
—⊟—	Truncation Error : x-momentum
—◇—	Truncation Error : y-momentum
—●—	Discretization Error : p
—■—	Discretization Error : u
—◆—	Discretization Error : v

FIG. 5.9. *Convergence of the L_1 norm of truncation and discretization errors observed in DS tests for the linear face-reconstruction FVD scheme with two types of straight-segment approximation to the curved tangency boundary.*

The linear face-reconstruction scheme possesses the flexibility to recover the 2nd-order accuracy with a straight-segment tangency boundary approximation. Two required modifications are illustrated in the sketch (b) of Figure 5.6: (1) the points P_B and P_C are moved to the boundary, and (2) the fluxes are reconstructed at the midpoints of the straight boundary segments, e.g., at $\bar{P} = 1/2P_B + 1/2P_0$. Figure 5.9 show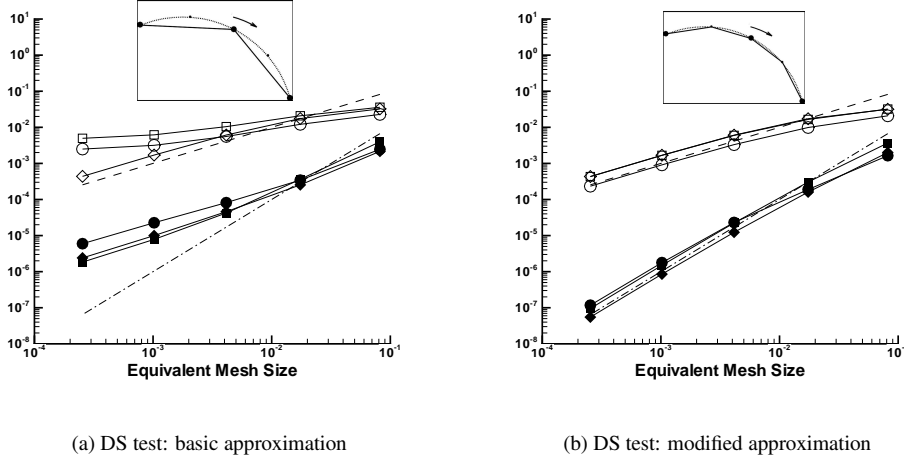s convergence of the L_1 norm of truncation and discretization errors observed in DS tests for the linear face-reconstruction FVD scheme with two types of straight-segment approximation to the curved tangency boundary: the basic median-dual approximation and the modified approximation. The tests are performed in the setting similar to the inflow/tangency boundary conditions used with the edge-reconstruction scheme. The results confirm that, with modifications (1) and (2), the 2nd-order convergence can be achieved with linear polynomials and a straight-segment approximation to the curved tangency boundary. Slower convergence observed with the basic median-dual cells indicates that both modifications are essential. Although not shown, with

the quadratic face-reconstruction scheme and a quadratic fit to the curved tangency boundary, discretization errors converge with the 3rd order.

5.3. Discretization error deterioration at stagnation. Local discretization accuracy deterioration may occur in the vicinity of stagnation or near other singularities in degenerated equations. To provide an insight into this phenomenon, we consider a one-dimensional symmetry-line nonlinear convection equation

$$uu_x = f \qquad (5.19)$$

linearized around the leading-edge stagnation solution for the flat-plate geometry ($u = -x$)

$$-x\partial_x^h \delta^u - \delta^u = g, \quad \delta^u(-1) = \delta_{\text{inflow}}, \qquad (5.20)$$

where ∂_x^h is a discrete derivative approximation; the same equation describes the tangency flow in the vicinity of the trailing-edge stagnation. The solution of (5.20) represents the discretization error, δ^u. The right-hand side g is $O(h^p)$ small for p^{th}-order discretizations and represents possible residual perturbations; the inflow condition, $\delta^u = 0$ defined at $x = -1$, may also contain an $\delta_{\text{inflow}} = O(h^p)$ error. The general solution of the initial-value problem (4.2) on the interval $x \in [0, 1]$ is given by

$$\delta^u = \delta^u_{\text{particular}}(x) + \frac{\delta^u_{\text{particular}}(-1) - \delta_{\text{inflow}}}{x}, \qquad (5.21)$$

where $\delta^u_{\text{particular}}(x)$ is a particular solution of the equation (5.20). The function $\delta^u_{\text{particular}}(x)$ and the constant δ_{inflow} are both $O(h^p)$ small. However, the discretization error δ^u grows as $O(1/x)$ in the vicinity of stagnation ($x = 0$) and locally becomes $O(h^{p-1})$.

Analysis of the equivalent linear operator performed for the inviscid equations is also capable of detecting the discretization-error deterioration. In the vicinity of stagnation, both velocity components become $O(h)$ small and the equivalent operator becomes

$$E(Q) = \begin{pmatrix} O(1) & O(1) & 0 \\ O(h) & O(h) & O(1) \\ O(h) & O(h) & O(1) \end{pmatrix}, \qquad (5.22)$$

cf. (5.10). Thus,

$$J^{-1}(Q) \sim E^{-1}(Q) = \begin{pmatrix} O(1) & O(h^{-1}) & O(h^{-1}) \\ O(1) & O(h^{-1}) & O(h^{-1}) \\ O(h) & O(1) & O(1) \end{pmatrix}. \qquad (5.23)$$

For the velocity discretization errors, the asymptotic order of $J^{-1}(Q)$ becomes $m_J = -1$, but for the discretization error in pressure, the asymptotic order remains the same as in the interior, $m_J = 0$, implying different orders of convergence for different variables at stagnation. To retain uniformly the same discretization-error convergence for all variables, one has to approximate the momentum conservation equations at stagnation with higher order than in the interior.

Discretization accuracy deterioration in the vicinity of stagnation is a universal phenomenon and expected for any discretization of the inviscid flow equations. In simulations,

25

the stagnation accuracy deterioration is rarely noticed and seldom correctly attributed because its effect is mostly visible far downstream of stagnation. At stagnation, the solution and all its derivatives are very small; therefore, in spite of increased relative discretization error, the absolute value of the local error, which is proportional to some derivative of the solution, does not exceed a typical error away from stagnation. Also, the effect disappears in the presence of the diffusion terms that prevent equation degeneration.

The discretization error generated at stagnation is amplified by the accelerated flow convecting the error downstream. For leading-edge stagnation, this error is convected along the tangency boundary, affects very few points, and is almost not observable in integral norms, such as L_1 and L_2 norms, but can be clearly detected in the L_∞ norm. At the trailing-edge stagnation, the generated discretization error is convected into the interior affecting a larger area. This may explain the difficulties observed in solution of the trailing edge flow problems, even for relatively benign geometries such as flat-plate, cylinder, or parabola.

In order to see accuracy order reduction more clearly, the DS test at stagnation needs to be adjusted to evaluate the relative discretization error, defined as $|E_d|\,/\,|Q|$, where, for computing the relative discretization error in the velocities, $|Q|_{vel} = \max\left(\sqrt{u^2 + v^2}\right)$ and, for the relative discretization error in the pressure, $|Q|_p = \max(p)$; maxima are taken over the DS-test domain. In fact, evaluation of discretization error is always required in the form of *relative* error, independent on the solution magnitude. Away from stagnation, the absolute and relative errors converge with the same orders because $|Q|_{vel} = O(1)$ and $|Q|_p = O(1)$; at stagnation, $|Q|_{vel} = O(h)$ and $|Q|_p = O(1)$.

Formulation	Error convergence at trailing-edge stagnation, $O\left(h^\alpha\right)$				
	DS test		Grid-refinement computations		
	Relative Discr. Error	Trunc. Error	Discr. Error		Trunc. Error
			L_1 norm	L_∞ norm	
Edge-reconstruction, irregular triangular grid	$u, v : \alpha = 1$ $p : \alpha = 2$	$\alpha = 1$	$1 < \alpha < 2$	$\alpha = 1$	$\alpha = 1$
Edge-reconstruction, mixed-element grid	$u, v : \alpha = 0$ $p : \alpha = 1$	$\alpha = 0$	$0 < \alpha < 1$	$\alpha = 0$	$\alpha = 0$
Linear face-reconstruction, mixed-element grid	$u, v : \alpha = 1$ $p : \alpha = 2$	$\alpha = 1$	$1 < \alpha < 2$	$u, v : \alpha = 1$ $p : 1 < \alpha < 2$	$\alpha = 1$
Quadratic face-reconstruction, mixed-element grid	$u, v : \alpha = 2$ $p : \alpha = 3$	$\alpha = 2$	$2 < \alpha < 3$	$\alpha = 2$	$\alpha = 2$

TABLE 5.2

Convergence of discretization and truncation errors for various irregular grid formulations of the 2D inviscid incompressible equations at the aft of the unit cylinder. A single entry of α in the table indicates it refers to all the variables (u, v, p). One order reduction in convergence of discretization errors for velocity components is clearly observed in DS tests and in the L_∞ norm of the discretization errors obtained in grid refinement (cf. Table 5.1); slowdown of L_1-norm convergence is also observed. Truncation errors converge with the same order as in the interior.

Table 5.2 summarizes the error convergence orders observed in computations at the aft of the unit cylinder. Each global grid is formed from an underlying regular quadrilateral grid spanning 120 degrees in θ (centered about the most downstream point on the cylinder surface) with extent $1 \leq r \leq 2.2$ in the radial direction; the grids are generated with $2^{n+3} + 1$ points in both the radial and circumferential directions, where $n = 0, 1, 2, 3, 4$. On each grid, the regular quadrangles are split randomly into a fully-triangular grid or a mixed-element grid, as discussed previously. The DS test is performed with independent grid generation and the focal point placed at the most downstream point on the cylinder.

26

The analytical estimates and the DS test accurately predict convergence order of truncation errors and one-order degradation of the L_∞ norm of discretization errors in the grid-refinement computations. The integral L_1 norm of the discretization error is less sensitive to the degradation; the error generated at stagnation is propagated along the streamline coming from the stagnation, and the interior areas far away from the streamline are little affected. Note also that a clear distinction between convergence of relative discretization errors in the velocities and pressure predicted by (5.23) is observed only in the DS tests; in the global grid refinement computations, the nonlinear interactions slow the convergence of discretization errors in pressure, although, the pressure errors remain much smaller than the velocity discretization errors on the same grids.

6. Discussion. A new computational analysis tool, downscaling (DS) test, has been introduced and applied for studying the convergence rates of truncation and discretization errors of finite-volume discretization (FVD) schemes on general irregular grids. The study shows that the design-order convergence of discretization errors can be achieved even when truncation errors exhibit a lower-order convergence or, in some cases, do not converge at all. The DS test is a general, efficient, accurate and practical tool, enabling straightforward extension of verification and validation to general unstructured grid formulations. It also allows separate analysis of the interior, boundaries, and singularities that could be useful even in structured-grid settings.

There are several new findings arising from the use of the DS test analysis. It was shown that the discretization accuracy of a common node-centered edge-reconstruction FVD scheme, known to be 2nd-order accurate for inviscid equations on triangular grids, degenerates to 1st order for mixed grids. Alternative node-centered face-reconstruction schemes have been presented and demonstrated to provide 2nd and 3rd order accuracies on mixed grids. The local accuracy deterioration at intersections of tangency and inflow/outflow boundaries has been demonstrated using DS tests tailored to examine the local behavior of the boundary conditions. The discretization-error order reduction within inviscid stagnation regions has been demonstrated. The accuracy deterioration is local, affecting mainly the velocity components, but applies to any order scheme. The result is somewhat surprising because the solution is so simple but analysis of the Jacobian operator along the stagnation streamline has provided insight into the phenomena.

In 2-D inviscid computations, the cost of computing residuals of the face-reconstruction discretizations is about twice as large as the cost of edge-reconstruction residuals because the face-reconstruction discretizations require a solution of the approximate Riemann problem at each dual-cell boundary segment (face); the edge-reconstruction discretization requires one Riemann solution per two connecting segments. The cost increase in 3D computations for general tetrahedral grids is much larger because multiple dual control-volume faces are adjacent to each primal-mesh edge. A dramatic cost reduction for face-reconstruction schemes is achieved by evaluating the dissipation at the midpoints of primal-mesh edges, in the same way as in the edge-reconstruction discretization, once for all adjacent dual segments/faces; unsplit flux contributions are still evaluated at the dual segments/faces. Also, as shown in [8], the cost of face-reconstruction FVD schemes on cell-centered grids is much lower.

On typical 2-D unstructured grids, where most nodes have at least five neighbors, a typical computational stencil for the quadratic face-reconstruction discretization has the same size as a stencil for the linear face-reconstruction scheme. The memory requirements for the quadratic discretization are about two times higher than for linear discretizations because a larger number of coefficients is stored at each control volume.

REFERENCES

[1] M. Aftosmis, D. Gaitonde, and T. S. Tavares, *Behavior of linear reconstruction techniques on unstructured meshes*, AIAA Journal, 33 (1995), pp. 2038–2049.

[2] W. K. Anderson and D. L. Bonhaus, *An implicit upwind algorithm for computing turbulent flows on unstructured grids*, Computers and Fluids, 23 (1994), pp. 1–21.

[3] T. J. Barth, *Numerical aspects of computing high-Reynolds number flow on unstructured meshes*, AIAA Paper 91-0721, 29-th AIAA Aerospace Science Meeting, Reno, NV, January 1991.

[4] T. J. Barth, *Recent developments in high-order k-exact reconstruction on unstructured meshes*, AIAA Paper 93-0668, 31-st AIAA Aerospace Science Meeting, Reno, NV, January 1993.

[5] W. J. Coirier, *An adaptively-refined, Cartesian, cell-based scheme for the Euler and Navier-Stokes equations*, NASA TM-106754, October 1994.

[6] M. Delanaye and Y. Liu, *Quadratic reconstruction finite volume schemes on 3D arbitrary unstructured polyhedral grids*, AIAA Paper 1999-3259, 14-th AIAA CFD Conference, Norfolk, VA, June 1999.

[7] B. Despres, *Lax theorem and finite volume schemes*, Math. Comp., 73(247) (2003), pp. 1203–1234.

[8] B. Diskin and J. L. Thomas, *Accuracy analysis for mixed-element finite-volume discretization schemes*, NIA Report 2007-08, August 2007.

[9] B. Diskin and J. L. Thomas, *Analysis of boundary conditions for factorizable discretizations of the Euler equations*, ICASE Report 2002-13, NASA CR-2002-211648, May 2002.

[10] M. B. Giles, *Accuracy of node-based solutions on irregular meshes*, 11-th International Conference on Numerical Methods in Fluid Dynamics, Hampton, VA, 1988, Lecture Notes in Physics, v. 323, D. L. Dwoyer, M. Y. Hussaini, and R.G Voigt, eds., pp. 273–277, Springer-Verlag, 1989

[11] A. C. Haselbacher, *A Grid-Transparent Numerical Method for Compressible Viscous Flow on Mixed Unstructured Meshes*, PhD thesis, Loughborough University, 1999.

[12] A. C. Haselbacher, J. J. McGuirk, and G. J. Page, *Finite-volume discretization aspects for viscous flows on mixed unstructured grids*, AIAA Journal, 37 (1999), p. 477.

[13] D. R. Lindquist and M. B. Giles, *A comparison of numerical schemes on triangular and quadrilateral meshes*, 11-th International Conference on Numerical Methods in Fluid Dynamics, Hampton, VA, 1988, Lecture Notes in Physics, v. 323, D. L. Dwoyer, M. Y. Hussaini, and R.G Voigt, eds., pp. 369–373, Springer-Verlag, 1989.

[14] J. Morrison and M. Hemsch, *Statistical analysis of CFD solutions from the third AIAA drag prediction workshop*, AIAA Paper 2007-0254, 45-th AIAA Aerospace Science Meeting and Exhibit, Reno, NV, January 2007.

[15] Ch. Hirsch, *Numerical computation of internal and external flows. Vol.1, Fundamentals of numerical discretization*, John Wiley & Sons, Inc., New York, NY, 1988.

[16] L. Krivodonova and M. Berger, *High-order accurate implementation of solid wall boundary conditions in curved geometries*, J. Comput. Phys., 211 (2006), pp. 492–512.

[17] R. E. Mineck, J. L. Thomas, and B. Diskin, *Analysis tools for CFD multigrid solvers*, AIAA Paper 2004-2532, 34-th AIAA CFD conference, Portland, OR, June 2004.

[18] C. Ollivier-Gooch, A. Nejat, and K. Michalack, *On obtaining high-order finite-volume solutions to the Euler equations on unstructured meshes*, AIAA Paper 2007-4194, 18-th AIAA CFD conference, Miami, FL, June 2007.

[19] M. Svärd and J. Nordström, *An accuracy evaluation of unstructured node-centered finite-volume methods*, NIA Report 2005-04, NASA CR-2006-214293, April 2006.

[20] P. J. Roache, *Verification and Validation in Computational Science and Engineering*, Hermosa, Albuquerque, NM, 1998.

[21] P. L. Roe, *Approximate Riemann solvers, parameter vectors, and difference schemes*, J. Comp. Phys., 43 (1981), pp. 357–372.

[22] P. L. Roe, *Error estimates for cell-vertex solutions of the compressible Euler equations*, ICASE Report 87-6, NASA CR-1987-178235, January 1987.

[23] A. Syrakos and A. Goulas, *Estimate of the truncation error of finite volume discretization of the Navier-Stokes equations on collocated grids*, App. Num. Math., 2 (1986), pp. 529–550.

[24] E. Turkel, *Accuracy of schemes with nonuniform meshes for compressible fluid flows*, App. Num. Math., 2 (1986), pp. 529–550.

[25] J. L. Thomas, B. Diskin, and C. L. Rumsey, *Towards Verification of Unstructured-Grid Solvers*, AIAA Paper 2008-0666, 46-th Aerospace Sciences Meeting & Exhibit, Reno, NV, January 2008.

Appendix A. Boundary conditions for the incompressible Euler FVD schemes.

For the edge-reconstruction FVD scheme near a curved boundary, the computational boundary is constructed as a piecewise straight line connecting the grid nodes located at the physical boundary. The control volume around a boundary node, P_0, (see Figure A.1) is closed with the boundary segments $[P_B, P_0]$ and $[P_0, P_C]$. The straight-line approximation $[P_0, P_2]$ provides a 2nd-order accuracy to the curved boundary segments connecting nodes
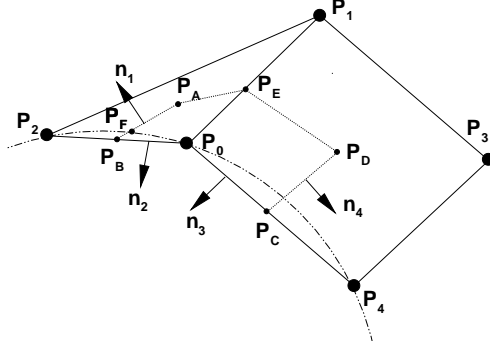
FIG. A.1. *Illustration for edge-reconstruction flux integration scheme near the boundary.*

P_0 and P_2. However, the approximation $[P_0, P_B]$ provides only a 1st-order accuracy for the $\widehat{P_0, P_F}$ part of the curved boundary segment. The flux reconstruction and integration over the segments $[P_A, P_E]$ and $[P_E, P_D]$ are the same as for the interior edges. The integral fluxes through segments $[P_A, P_B]$ and $[P_D, P_C]$ are approximated by the numerical fluxes (5.12) evaluated at points P_B and P_C using the directed areas $\mathbf{n}_1$ and $\mathbf{n}_4$, respectively. The linear solution approximation at control volumes ensures 2nd-order flux reconstruction accuracy.

Boundary conditions are enforced weakly through the boundary fluxes. At the inflow, where velocity components are specified through prescribed boundary conditions, the boundary flux uses the specified velocities, the pressure is reconstructed from the discrete solution approximation. The outflow conditions are implemented similarly: the pressure contribution to the boundary flux is specified from prescribed conditions; the velocity components are reconstructed from the discrete solution. At the tangency boundary, the mass fluxes and velocity contributions to the momentum fluxes are explicitly set to zero; the pressure is reconstructed from the discrete solution.

On triangular grids, the integral flux through the boundary segment $[P_B, P_0]$ is computed as $\left(\mathbf{F^h}_{[P_B, P_0]} \cdot \mathbf{n}_2\right)$, where $\mathbf{n}_2$ is the directed area of $[P_B, P_0]$, and $\mathbf{F^h}_{[P_B, P_0]}$ is evaluated at $\bar{P} = 5/6 P_0 + 1/6 P_2$. The solution components prescribed in the boundary conditions, e.g., both velocities at inflow, or the pressure at outflow, are specified at $\bar{P}$ from the known exact solution; other components are interpolated to $\bar{P}$ from the endpoints of the segment $[P_2, P_0]$. The integral flux through $[P_0, P_C]$ is computed analogously. In spite of providing only 1st-order local accuracy for integrated fluxes through $[P_B, P_0]$ and $[P_0, P_C]$, the coefficients $5/6$ and $1/6$ lead to cancellation of 1st-order errors, providing zero residuals for conservation laws with linear fluxes and, thus, supporting the global 2nd-order flux integration accuracy [3].

On mixed-element and irregular-quadrilateral grids, the 2nd-order flux integration accuracy is not recovered. For triangular cells adjacent to the boundary, the $(5/6, 1/6)$ rule is still enforced; on the boundary segments of quadrilateral cells, the fluxes are evaluated at the segment midpoint, $\bar{P} = 3/4 P_0 + 1/4 P_2$. The overall boundary approximation accuracy for $R(Q)$ is consistent with the accuracy of the interior FVD scheme, 2nd order for triangular grids and 1st order for other irregular grids.

Reliance on error cancellation in providing design-order discretization accuracy may lead to some counterintuitive phenomena. In particular, improving the accuracy of boundary con-

29

ditions in a way that is not compatible with the flux computations through interior segments can upset the error cancellation balance and, in fact, worsen approximation accuracy of $R(Q)$, at least, locally. In some cases, this local imbalance is compensated by contributions from other boundary segments. The imbalance is especially prominent at the corners where the boundary segments represent different types (e.g., tangency and inflow) of boundaries.

For control volumes at general curved tangency boundaries, the tangency condition is enforced over the straight segments, rather than over the physical curved boundary. The error introduced by this approach can be considered as a flux reconstruction error introduced by enforcing zero velocity over non-tangency boundary segments. As estimated analytically and confirmed numerically in Section 5.2.4, the error is $O(h)$ for each segment of the tangency boundary. Reference [16] investigates an alternative approach, in which other types of boundary conditions are enforced over the straight boundary segments approximating a curved tangency boundary.

The boundary conditions for the face-reconstruction discretizations are also enforced weakly, through boundary fluxes. At inflow and outflow, the computational domain has a piecewise straight boundary; the solution components are either specified from the exact solution (the velocity is specified at inflow and the pressure is specified at outflow) or represented by the polynomial approximation defined at the adjacent control volume. At tangency, the 2nd-order accuracy can still be achieved with enforcing tangency over piecewise linear segments. (See discussion in Section 5.2.4.) For the 3rd-order accuracy, the physical boundary should be approximated quadratically. In a general case, where the analytical shape of the boundary is unknown, the boundary should be represented as a piecewise polynomial curve providing the required accuracy for the boundary shape.